Analytical Modeling of Open-Circuit Air-Gap Flux Density in Interior Permanent Magnet Machine

Haijun Zhuang[1], Shuguang Zuo[1], Zhixun Ma[2], Qiang Yu[3], Zhipeng Wu[1], and Chang Liu[1]

[1]School of Automotive Studies, Tongji University, Shanghai 201804, China
[2]National Maglev Transportation Engineering Research and Development Center, Tongji University, Shanghai 201804, China
[3]School of Information and Control Engineering, China University of Mining and Technology, Xuzhou 221116, China

In this article, a general analytical model suitable for the magnetic analysis of the interior permanent magnet (IPM) machine is proposed by coupling the equivalent model and Maxwell's equation-based 3-D analytical model. In the proposed analytical model, to reduce boundary conditions, the IPM topology is transformed into the surface-mounted permanent magnet (SPM) topology through the equivalent model with universality. Meanwhile, Maxwell's equation-based 3-D analytical model is established to conduct magnetic analysis and then gives a unified expression of air-gap flux density of the IPM machine. Then, the saliency effect is considered using the saliency coefficient, which is deduced by the magnetomotive force (MMF) and flux-path permeance model. In addition, the slotting effect is considered by conformal mapping. The saliency and slotting effect act on additional functions in the analytical model. Finally, the accuracy of the analytical method is validated by the finite-element method (FEM) in the IPM machine condition.

Index Terms— Analytical model, interior permanent magnet (IPM) machine, saliency effect, slotting effect.

I. INTRODUCTION

DUE to high power density, high efficiency, and wide speed range, an interior permanent magnet (IPM) synchronous machine is widely used in the electric vehicle drive domain [1], [2]. In the harsh operating environment of the electric vehicle, the smaller air-gap length can aggravate flux density variation, which ultimately results in noise and vibration [3], [4], [5]. Meanwhile, based on the open-circuit air-gap flux density, a deal of significant electromagnetic characteristics can be obtained, such as cogging torque and back electromagnetic force [6], [7]. Therefore, the accurate and fast prediction of air-gap flux density for the IPM machine is essential.

Finite-element method (FEM), with high precision of results, is widely used in the electromagnetic analytical domain [8], [9]. However, the sensitivity of the air-gap magnetic field requires precise calculations, which makes the solution time-consuming. Therefore, the semi-numerical method is presented to reduce computational time [10]. However, FEM is not competent to investigate the electromagnetic characteristics.

The analytical method, as another means to calculate the electromagnetic characteristics, is also widely used in the early stage of motor design because of its rapidity and accuracy. Analytical methods mainly include the magnetic equivalent circuit (MEC) and Maxwell's equation-based analytical model. For MEC, the elements are magnetomotive force (MMF) and magnetic reluctance, which depends on machine structure

parameters and flux path. In [11] and [12], the MEC model is established for the IPM machine to calculate stator iron loss. However, due to the over-simplification of the reluctance, the calculation accuracy is barely satisfactory. To pursue accuracy, a novel network-based MEC model is proposed, which concentrates on air-gap permeance modeling and modular model establishment [13]. Therefore, the accuracy of MEC depends on the reluctance division and the number of circuits. However, a uniform expression of air-gap flux density cannot be obtained by MEC, which is not conducive to analyzing the spatial and temporal order characteristics of electromagnetic force. Furthermore, electromagnetic vibration and noise cannot be effectively investigated. To solve this problem, Maxwell's equation-based analytical model is built, and electromagnetic characteristics are calculated by the magnetic potential vector. In this analytical model, each part of the motor is electromagnetically independent and linked by boundary conditions. For the surface-mounted permanent magnet (SPM) machine, the air-gap flux density is particularly deduced in polar coordinates by Zhu et al. [14]. For the magnetically geared permanent magnet (PM) machine, the 2-D analytical model is utilized to conduct magnetic analysis of electromagnetic characteristics [15]. For the canned switched reluctance machine, the multi-layer analytical model is utilized to conduct the canned effect analysis [16]. In this analytical model, the author focuses on modeling MMF of the current. However, as to the electromagnetic analysis of IPM machines, Maxwell's equation-based analytical model is not directly effective. This is because of the numerous boundary condition. Therefore, in [17], the IPM rotor topology is equivalent to the SPM rotor topology, and the saliency and slotting effect are considered through conformal mapping in polar coordinates. However, in the equivalent process, the thickness of the PM is constant, which leads to a large amplitude of MMF. Therefore, the flux density of this analytical model has a certain error
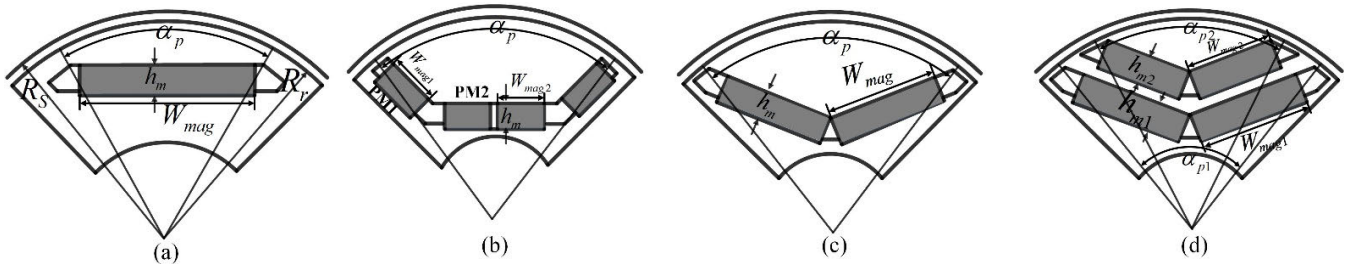
Fig. 1. Rotors of the IPM machines. (a) Tangentially IPM. (b) Multi-segment tangentially IPM. (c) Single-layer V-shaped IPM. (d) Double-layer V-shaped IPM.

with that of FEM. Currently, for Maxwell's equation-based analytical model, most of the literature is 2-D and focuses on the SPM machine. However, the axial segmented technique is widely used in driving motors in electric vehicles to improve output performances, such as skewed slots or poles [18], [19]. For machines with the axial segmented technique, the air-gap flux density distribution changes with axial position variation, leading to different electromagnetic forces acting on each segment. Therefore, the 3-D distribution characteristics of vibration and noise are difficult to be investigated through a 2-D analytical model. This is because the distributed force needs to be mapped and loaded along the axial direction. Hence, a general analytical model needs to be established to conduct the magnetic analysis of IPM machines, regardless of rotor topology and axial topology.

Due to the slot, the air-gap flux density is modulated and yields new harmonic orders. Therefore, the slotting effect should be considered. As to the slotting effect, sub-domain model and conformal mapping are two widely accepted models. For conformal mapping, in [20], the complex relative permeance function is proposed, and the slotted air-gap flux density is obtained by multiplying the non-slotted air-gap flux density by the permeance function. However, the general expression of the complex relative permeance function is not given. Therefore, in [21], an analytical method is proposed to conduct the general expression of the complex relative permeance function. For the sub-domain analytical model, the slotting effect is considered during the air-gap flux density solution process. The slot, stator yoke, and stator teeth are seen as sub-domains with adjacent boundary conditions [22]. However, the excessive introduction of boundary conditions enhances the complexity of the solution process. Therefore, to calculate the slotting effect accurately and conveniently, an analytical model based on MMF and flux-path permeance function is proposed [23].

In this article, a general analytical model is proposed for the IPM machine by coupling the equivalent rotor model and Maxwell's equation-based 3-D analytical model, which is suitable for any rotor topology and axial topology. Meanwhile, the saliency effect and slotting effect work as additional functions on the analytical model. The organization is given as follows. In Section II, the principle and universality of the rotor equivalent model are illustrated in detail. In Section III, Maxwell's equation-based 3-D analytical model is built, and then, the uniform expressions of electromagnetic characteristics are deduced. In Section IV, the effectiveness of magnetic analysis

is verified by the FEM. In Section V, the saliency effect and slotting effect are investigated.

II. EQUIVALENT ROTOR TOPOLOGY MODEL

In order to illustrate the universality of the equivalent rotor topology model, four typical IPM topologies are chosen as studied machines, which are shown in Fig. 1. Four IPM topologies are tangentially IPM, multi-segment tangentially IPM, single-layer V-shaped PM, and double-layer V-shaped PM. They have the same stator structure, and the only difference exists in the IPM structure. Then, the meanings of the structural parameters of four IPM machines in Fig. 1 are shown in Tables II–IV.

The analytical modeling of the magnetic field in IPM machines is derived based on the following assumptions.

1) The permeability of iron parts is infinite.

2) The magnet property of IPM and equivalent SPM is linear.

3) The slotting effect is omitted.

4) The flux leakage and saturation are neglected.

Under the premise of ignoring flux leakage and saturation, lumped magnetic circuits related to rotor topologies are shown in Fig. 2. For single-layer IPM, through the stator yoke, air gap, PMs, and rotor yoke, the main flux loop is formed. Therefore, relevant lumped magnetic circuits are shown in Fig. 2(a)–(c), where R_g and R_m represent the air-gap reluctance and magnet reluctance, respectively. Meanwhile, F_m denotes the MMF of PM. For MMF, since PM has a straight second quadrant demagnetization curve, the amplitude can be calculated as

$$\Theta_{\text{PM}} = k_{\text{mag}} \cdot H_c \cdot h_m \tag{1}$$

$$k_{\text{mag}} = W_{\text{mag}}/W'_{\text{mag}} \tag{2}$$

where W'_{mag} is the width of the equivalent SPM and k_{mag} represents the equivalent coefficient of MMF. For SPM rotor topology, $k_{\text{mag}} = 1$. H_c is the coercive field intensity of PM material.

Meanwhile, in terms of reluctance, magnet reluctance and air-gap reluctance can be calculated as

$$R_m = h_m/\mu_0 \tag{3}$$

$$R_g = g/\mu_0 \tag{4}$$

where μ_0 is the permeability of the vacuum.

For the double-layer IPM, the superposition principle is utilized, i.e., each layer of IPM can be regarded as an independent
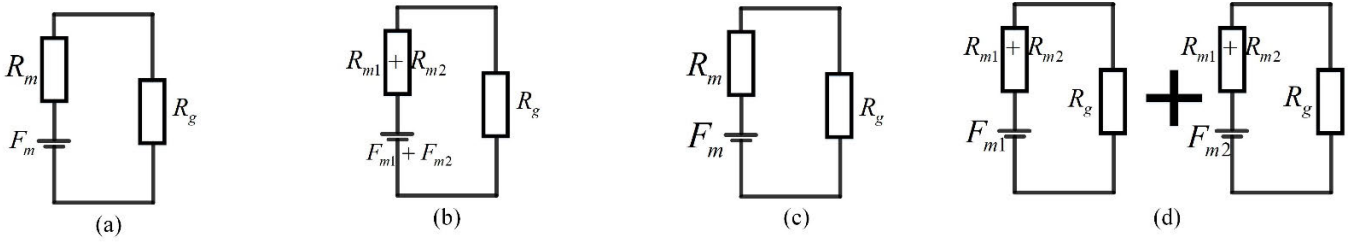
Fig. 2. Rotor MEC of IPM machines. (a) Tangentially IPM. (b) Multi-segment tangentially IPM. (c) Single-layer V-shaped PM. (d) Double-layer V-shaped PM.
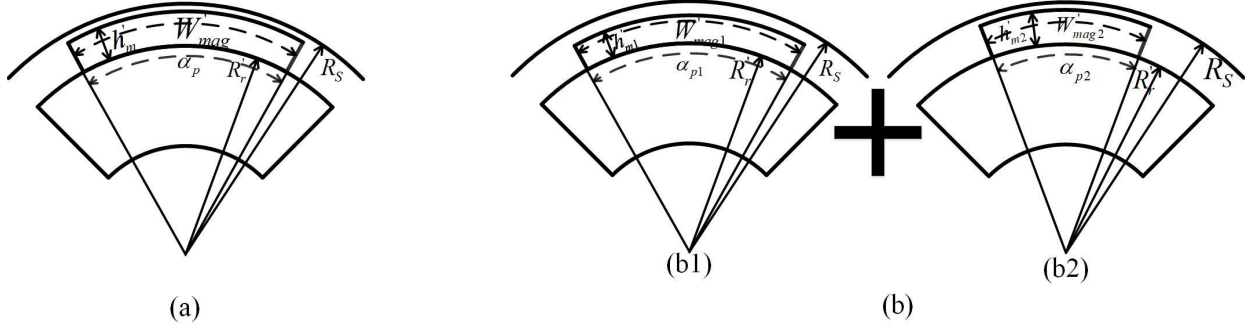

Fig. 3. Equivalent rotor of IPM machines. (a) Single-layer. (b1) and (b2) Double-layer.

magnetic source. Therefore, the relevant magnetic circuit is shown in Fig. 2(d). The superposition principle is justified because of infinite permeable of iron parts and linear magnet property of PMs, which make the system linear.

Depending on the lumped magnetic circuit, the IPM rotor topology can be transformed into the SPM rotor topology to reduce complex boundary conditions. Meanwhile, the equivalent principle is constant MMF and reluctance. It should be noted that: 1) the equivalent SPM is radially magnetized and 2) the pole-arc width of four IPM topologies keeps constant before and after equivalent process. Meanwhile, the magnet pole-arc width includes the parameters of PM and the rib. Then, the equivalent SPM topology for single-layer IPM is shown in Fig. 3(a). For the single-layer IPM, in order to keep the amplitude of MMF constant, the thickness of equivalent SPM needs to be changed, which can be expressed as (5). In order to keep the reluctance constant, the sum of the thickness of PM and the air gap remains unchanged before and after the equivalent process, which can be expressed as (6). According to the following equations, the equivalent SPM structural parameters can be calculated:

$$h_m \cdot W_{\mathrm{mag}} = \frac{1}{2} \cdot \left(\alpha_p \cdot \frac{\pi}{p}\right) \cdot \left[(R'_r + h'_m)^2 - R'^2_r\right] \quad (5)$$

$$\begin{cases} h_m + g = h'_m + g' \\ R'_r + g' + h'_m = R_r + g. \end{cases} \quad (6)$$

In analogy, the equivalent SPM for double-layer IPM is shown in Fig. 3(b). Since each layer of IPM is an independent magnetic circuit, each layer of IPM can be correspondingly equivalent to an SPM, and its structural parameters are obtained according to (5) and (6). Therefore, the air-gap flux density under the double-layer IPM excitation is the
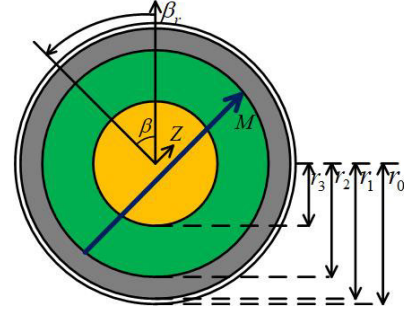

Fig. 4. Maxwell's equation-based 3-D analytical model.

linear superposition of that under each-layer equivalent SPM excitation.

III. ANALYTICAL CALCULATION MODEL

To perform the magnetic analysis of the equivalent SPM machine, Maxwell's equation-based 3-D analytical model is built, as shown in Fig. 4, which is calculated in the cylindrical coordinate system. The multi-layer concentric cylinder is the prominent characteristic of the analytical model, which consists of the air-gap layer, PM layer, rotor layer, and shaft layer. Since the magnetic permeability of the stator core is assumed to be infinite, the stator layer can be omitted and only boundary conditions exist. Meanwhile, the neglected slotting effect is considered by conformal mapping, which works as an additional function on the analytical model. Next, the upright direction represents the starting point, and the direction of rotation of the rotor is counterclockwise. Meanwhile, β_r represents the fixed rotor coordinate system.

In Fig. 4, each layer is numbered. $i = 1$ represents the air-gap layer and so on, up to the shaft layer. The subscript r represents the radius of the corresponding layer.
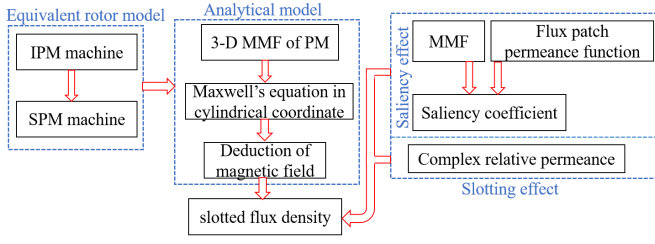
Fig. 5. Flowchart of the analytical model.

In order to illustrate analytical modeling, Fig. 5 shows the flow of the analysis, with three steps. The first step is the conversion of the IPM topology to the SPM topology, which has been completed in Section II. In the second step, the 3-D analytical model is established. The calculation method is organized as follows. Starting from the MMF distribution of PM in Section III-A, the deduction of the magnetic field is performed in Sections III-B and III-C. In the third step, the saliency effect is considered to revise non-slotted tangential flux density, and then, the slotted air-gap flux density is investigated by the complex relative permeance.

A. MMF Calculation

For the equivalent SPM, the residual magnetization vector $\overrightarrow{M}$ in the cylindrical coordinates can be calculated by

$$\overrightarrow{M} = M_r \overrightarrow{e_r} + M_\beta \overrightarrow{e_\beta} \tag{7}$$

where M_r and M_β are the radial and tangential components of magnetization, respectively, which can be demonstrated in Fig. 6.

The distribution of radial and tangential components of the residual magnetization vector is shown in Fig. 6(c) and (d), respectively. Due to the radial magnetizing direction of equivalent SPM, the amplitude of M_β is equal to zero. Meanwhile, the radial component can be expressed by the Fourier series as

$$M_r(\beta) = \sum_\xi {}^\xi M_r \cdot e^{-j\xi\beta} \quad \xi = 1, 3, 5 \dots \tag{8}$$

$${}^\xi M_r = 2 \frac{B_{\text{rem}}}{\mu_0} \alpha_p \frac{\sin\left(\frac{\xi\pi\alpha_p}{2}\right)}{\frac{\xi\pi\alpha_p}{2}} \tag{9}$$

where ξ is the circumferential harmonic order and B_{rem} is the remanence. β is the electrical angle, which can convert to the mechanical angle by $\beta = p\alpha$, where p is the number of pole pairs and α is the mechanical angle.

The axial distribution of magnetization is shown in Fig. 7. Then, the function $f(z)$ can also be expressed by the Fourier series as

$$f(z) = 2 \sum_\kappa \frac{\sin\left(\frac{\kappa\pi}{2}\right)}{\frac{\kappa\pi}{2}} \cos\left(\frac{\kappa\pi}{L}z\right) = \sum_\kappa {}^\kappa a \cos\left(\frac{\kappa\pi}{L}z\right) \tag{10}$$

$${}^\kappa a = 2 * \frac{\sin\left(\frac{\kappa\pi}{2}\right)}{\frac{\kappa\pi}{2}}, \quad \kappa = 1, 3, 5, \dots \tag{11}$$

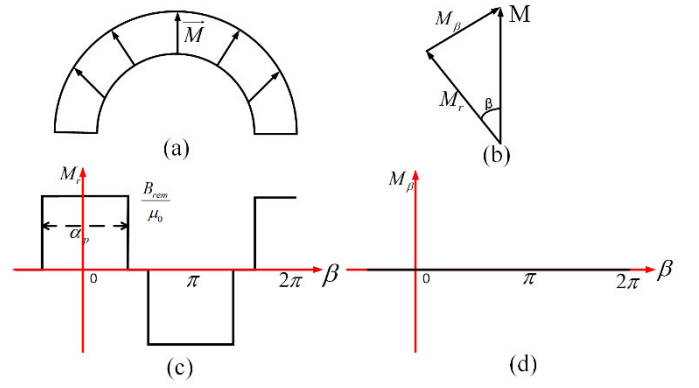where κ is the axial harmonic order.

Fig. 6. Residual magnetization vector model. (a) Radial magnetizing model. (b) Residual magnetization vector model. (c) Distribution of radial magnetization. (d) Distribution of tangential magnetization.

Therefore, 3-D magnetization with radial magnetization can be expressed as

$${}^{\xi,\kappa}\overrightarrow{M}(\beta, z) = {}^\xi M_r(\beta) \overrightarrow{e}_r \cdot f(z). \tag{12}$$

B. Maxwell's Equation

In Maxwell's equation-based 3-D analytical model, magnetic vector potential is used to conduct the electromagnetic analysis. Due to the radial magnetizing direction, the equivalent bulk current flows in the axial and circumferential direction, i.e., $A_r = 0$. However, due to the existent PM, Poisson's equations have different forms in different layers.

For layers without PM, Poisson's equation can be expressed as

$$\begin{cases} \dfrac{1}{r}\dfrac{\partial}{\partial r}{}^{\xi,\kappa}A_{\beta,i} + \dfrac{\partial^2}{\partial r^2}{}^{\xi,\kappa}A_{\beta,i} + \dfrac{1}{r^2}\dfrac{\partial^2}{\partial\beta^2}{}^{\xi,\kappa}A_{\beta,i} + \dfrac{\partial^2}{\partial z^2}{}^{\xi,\kappa}A_{\beta,i} \\ \qquad = \mu_i\gamma_i\dfrac{\partial}{\partial t}{}^{\xi,\kappa}A_{\beta,i} \\ \dfrac{1}{r}\dfrac{\partial}{\partial r}{}^{\xi,\kappa}A_{z,i} + \dfrac{\partial^2}{\partial r^2}{}^{\xi,\kappa}A_{z,i} + \dfrac{1}{r^2}\dfrac{\partial^2}{\partial\beta^2}{}^{\xi,\kappa}A_{z,i} + \dfrac{\partial^2}{\partial z^2}{}^{\xi,\kappa}A_{z,i} \\ \qquad = \mu_i\gamma_i\dfrac{\partial}{\partial t}{}^{\xi,\kappa}A_{z,i} \end{cases} \tag{13}$$

where μ_i and γ_i are the recoil permeability and the conductivity, respectively.

For the PM layer, due to the existing magnetization, Poisson's equation can be expressed as

$$\begin{cases} \dfrac{1}{r}\dfrac{\partial}{\partial r}{}^{\xi,\kappa}A_{\beta,i} + \dfrac{\partial^2}{\partial r^2}{}^{\xi,\kappa}A_{\beta,i} + \dfrac{1}{r^2}\dfrac{\partial^2}{\partial\beta^2}{}^{\xi,\kappa}A_{\beta,i} + \dfrac{\partial^2}{\partial z^2}{}^{\xi,\kappa}A_{\beta,i} \\ \qquad = \mu\gamma\dfrac{\partial}{\partial t}{}^{\xi,\kappa}A_{\beta,i} - \mu_0\dfrac{\partial}{\partial z}{}^{\xi,\kappa}M_{r,z} \\ \dfrac{1}{r}\dfrac{\partial}{\partial r}{}^{\xi,\kappa}A_{z,i} + \dfrac{\partial^2}{\partial r^2}{}^{\xi,\kappa}A_{z,i} + \dfrac{1}{r^2}\dfrac{\partial^2}{\partial\beta^2}{}^{\xi,\kappa}A_{z,i} + \dfrac{\partial^2}{\partial z^2}{}^{\xi,\kappa}A_{z,i} \\ \qquad = \mu\gamma\dfrac{\partial}{\partial t}{}^{\xi,\kappa}A_{z,i} + \mu_0\dfrac{1}{r}\dfrac{\partial}{\partial\beta}{}^{\xi,\kappa}M_{r,z}. \end{cases} \tag{14}$$

Due to the nonexistent stator current in the open-loop analysis, the magnetic vector potential can be fixed in rotor coordinates and does not change with time, which results in the amplitude of $\partial/\partial t\,{}^{\xi,\kappa}A$ becoming zero. Then, for the
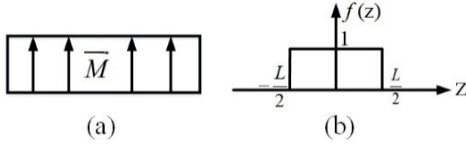
Fig. 7. Axial distribution of magnetization. (a) Axial distribution of magnetization model. (b) Axial distribution function of magnetization.

z-component of the magnetic vector potential in layers without PM, Poisson's equation can be expressed as

$$\frac{1}{r}\frac{\partial}{\partial r}{}^{\xi,\kappa}A_{z,i} + \frac{\partial^2}{\partial r^2}{}^{\xi,\kappa}A_{z,i} + \frac{1}{r^2}\frac{\partial^2}{\partial \beta^2}{}^{\xi,\kappa}A_{z,i} + \frac{\partial^2}{\partial z^2}{}^{\xi,\kappa}A_{z,i} = 0. \tag{15}$$

To solve Poisson's equation, the method of separation of variables is applied. For the first layer, as an example, the solution of the z-component of the magnetic vector potential can be expressed as

$$^{\xi,\kappa}A_{z,1} = {}^{\xi}\lambda_1(\beta) \cdot {}^{\xi,\kappa}R_1(r) \cdot {}^{\kappa}Z_1(z) \tag{16}$$

where ${}^{\xi}\lambda_1(\beta)$ and ${}^{\kappa}Z_1(z)$ are, respectively, circumferential and axial components of the MMF and ${}^{\xi,\kappa}R_1(r)$ refers to the radius of air gap. Furthermore, ${}^{\xi}\lambda_1(\beta)$ and ${}^{\kappa}Z_1(z)$ can be expressed as

$$^{\xi}\lambda_1(\beta) = {}^{\xi}C_1 \cdot e^{-j\xi\beta} \tag{17}$$

$$^{\kappa}Z_1(z) = {}^{\kappa}C_2 \cdot {}^{\kappa}a \cdot e^{-j\kappa\frac{\pi}{L}z} \tag{18}$$

where ${}^{\xi}C_1$ and ${}^{\kappa}C_2$ are the constant coefficients of the circumferential and axial components, respectively

$$^{\xi}\lambda_1'' = -\xi^2 \cdot {}^{\xi}\lambda_1 \tag{19}$$

$$^{\kappa}Z_1'' = -\left(\kappa\frac{\pi}{L}\right)^2 {}^{\kappa}Z_1. \tag{20}$$

Due to (19) and (20), we can get

$$r^2 \cdot {}^{\xi,\kappa}R_1'' + r \cdot {}^{\xi,\kappa}R_1' - \left({}^{\kappa}k_1^2 \cdot r^2 + \xi^2\right) \cdot {}^{\xi,\kappa}R_1 = 0 \tag{21}$$

$$^{\kappa}k_1^2 = \left(\kappa\frac{\pi}{L}\right)^2 \tag{22}$$

where (21) is the modified Bessel's differential equation of the ξth order. Due to the integral amplitude of ξ, the general solution of this differential equation is

$$^{\xi,\kappa}R_1(r) = {}^{\xi,\kappa}C_3 \cdot I_\xi({}^{\kappa}k_1 \cdot r) + {}^{\xi,\kappa}C_4 \cdot K_\xi({}^{\kappa}k_1 \cdot r) \tag{23}$$

where I_ξ is the modified Bessel function of the first kind and K_ξ is the modified Bessel function of the second kind; the coefficients ${}^{\xi,\kappa}C_3$ and ${}^{\xi,\kappa}C_4$ are constant.

Equations (17), (18), and (23) are substituted into (16), and thus, the z-component of the magnetic vector potential can be obtained

$$^{\xi,\kappa}A_{z,1} = {}^{\xi,\kappa}C_5\left[I_\xi({}^{\kappa}k_1 \cdot r) + {}^{\xi,\kappa}C_6 \cdot K_\xi({}^{\kappa}k_1 \cdot r)\right]$$
$$\cdot {}^{\kappa}a \cdot \cos\left(\kappa\frac{\pi}{L}z\right) \cdot e^{-j\xi\beta}. \tag{24}$$

Due to $\text{div}(A) = 0$, we can get

$$\frac{\partial}{\partial z}A_z + \frac{1}{r}\frac{\partial}{\partial \beta}A_\beta = 0. \tag{25}$$

According to (25), the β-component the magnetic vector potential can be expressed as

$$^{\xi,\kappa}A_{\beta,1} = j\frac{r}{\xi}\frac{\kappa\pi}{L} \cdot {}^{\xi,\kappa}C_5\left[I_\xi({}^{\kappa}k_1 \cdot r) + {}^{\xi,\kappa}C_6 \cdot K_\xi({}^{\kappa}k_1 \cdot r)\right]$$
$$\cdot {}^{\kappa}a \sin\left(\kappa\frac{\pi}{L}z\right) \cdot e^{-j\xi\beta}. \tag{26}$$

Similarly, for the rotor core without magnetization, the magnetic vector potential can be expressed as

$$^{\xi,\kappa}A_{z,3} = {}^{\xi,\kappa}C_9\left[I_\xi({}^{\kappa}k_3 \cdot r) + {}^{\xi,\kappa}C_{10} \cdot K_\xi({}^{\kappa}k_3 \cdot r)\right]$$
$$\cdot {}^{\kappa}a \cos\left(\kappa\frac{\pi}{L}z\right) \cdot e^{-j\xi\beta} \tag{27}$$

$$^{\xi,\kappa}A_{\beta,3} = j\frac{r}{\xi}\frac{\kappa\pi}{B} \cdot {}^{\xi,\kappa}C_9\left[I_\xi({}^{\kappa}k_3 \cdot r) + {}^{\xi,\kappa}C_{10} \cdot K_\xi({}^{\kappa}k_3 \cdot r)\right]$$
$$\cdot {}^{\kappa}a \sin\left(\kappa\frac{\pi}{L}z\right) \cdot e^{-j\xi\beta}. \tag{28}$$

For $i = i_{\max,\max-1}$

$$^{\xi,\kappa}C_{10} = 0. \tag{29}$$

Therefore, (27) and (28) are transformed as

$$^{\xi,\kappa}A_{z,3} = {}^{\xi,\kappa}C_9 \cdot I_\xi({}^{\kappa}k_3 \cdot r) \cdot {}^{\kappa}a \cos\left(\kappa\frac{\pi}{L}z\right) \cdot e^{-j\xi\beta} \tag{30}$$

$$^{\xi,\kappa}A_{\beta,3} = j\frac{r}{\xi}\frac{\kappa\pi}{B} \cdot {}^{\xi,\kappa}C_9 \cdot I_\xi({}^{\kappa}k_3 \cdot r) \cdot {}^{\kappa}a \sin\left(\kappa\frac{\pi}{L}z\right) \cdot e^{-j\xi\beta}. \tag{31}$$

For the PM layer, Poisson's equation for the z-component of the magnetic vector potential can be calculated as

$$\frac{1}{r}\frac{\partial}{\partial r}{}^{\xi,\kappa}A_{z,i} + \frac{\partial^2}{\partial r^2}{}^{\xi,\kappa}A_{z,i} + \frac{1}{r^2}\frac{\partial^2}{\partial \beta^2}{}^{\xi,\kappa}A_{z,i} + \frac{\partial^2}{\partial z^2}{}^{\xi,\kappa}A_{z,i}$$
$$= -j\frac{\mu_0}{r} \cdot {}^{\xi,\kappa}M^\Delta \cdot e^{-j\xi\beta} \tag{32}$$

where ${}^{\xi,\kappa}M^\Delta$ is the magnetization differential expression, which can be expressed as

$$^{\xi,\kappa}M^\Delta = \xi \cdot {}^{\xi}M_r \cdot {}^{\kappa}a \cdot \cos\left(\kappa\frac{\pi}{L}\right). \tag{33}$$

The method of separation of variables is also used in solving Poisson's equation, so we can get

$$r^2 \cdot {}^{\xi,\kappa}R_2'' + r \cdot {}^{\xi,\kappa}R_2' - \left({}^{\kappa}k_2^2 \cdot r^2 + \xi^2\right) \cdot {}^{\xi,\kappa}R_2 = r \tag{34}$$

which is a nonhomogeneous modified Bessel's differential equation. The general solution of the nonhomogeneous can be written as

$$^{\xi,\kappa}R_2 = {}^{\xi,\kappa}R_{2H} + {}^{\xi,\kappa}R_{2P} \tag{35}$$

where ${}^{\xi,\kappa}R_{2H}$ and ${}^{\xi,\kappa}R_{2P}$ are the homogenous and particular solutions of the differential equation.

The homogenous solution can be expressed as

$$^{\xi,\kappa}R_{2H} = {}^{\xi,\kappa}C_7 \cdot I_\xi({}^{\kappa}k_2 \cdot r) + {}^{\xi,\kappa}C_8 \cdot K_\xi({}^{\kappa}k_2 \cdot r). \tag{36}$$

For different orders, the particular solution has different expressions, but it can be derived as
for $\xi = 1$

$$^{\xi,\kappa}R_{2P} = -\frac{1}{{}^{\kappa}k_2}\left[\begin{array}{l} I_1({}^{\kappa}k_2 \cdot r) \cdot K_0({}^{\kappa}k_2 \cdot r) \\ +K_1({}^{\kappa}k_2 \cdot r) \cdot I_0({}^{\kappa}k_2 \cdot r) \end{array}\right]. \tag{37}$$

For $\xi = 3, 5, 7, \ldots$, the equation is shown in (38), at the bottom of the page.

Therefore, for the PM layer, the z-component of the magnetic vector potential can be expressed as

$$^{\xi,\kappa}A_{z,2} = -j\mu_0 \cdot {}^{\xi,\kappa}M^{\Delta} \cdot \left[{}^{\xi,\kappa}R_{2H} + {}^{\xi,\kappa}R_{2P}\right] \cdot e^{-j\xi\beta}. \quad (39)$$

Due to the curly relation of the magnetic vector potential, the β-component can be expressed as

$$^{\xi,\kappa}A_{\beta,2} = \mu_0 \frac{r}{\xi} \cdot \frac{\kappa\pi}{L} {}^{\xi,\kappa}M^{\otimes} \cdot \begin{bmatrix} {}^{\xi,\kappa}R_{2H} \\ +{}^{\xi,\kappa}R_{2P} \end{bmatrix} \cdot e^{-j\xi\beta} \quad (40)$$

where $^{\xi,\kappa}M^{\otimes}$ is the magnetization differential expression, which can be expressed as

$$^{\xi,\kappa}M^{\otimes} = {}^{\xi}M_r \cdot {}^{\kappa}a \cdot \sin\left(\kappa\frac{\pi}{L}\right). \quad (41)$$

C. Calculation of C_i Constant

Due to the nonexistent stator current, for different layers, the boundary conditions in terms of the tangential component of field strength and the normal component of flux density are constant, which can be expressed as

$$H_{\beta,1}(r, \beta, z)\big|_{r=r_0} = 0$$
$$\begin{cases} H_{\beta,1}(r, \beta, z)\big|_{r=r_1} = H_{\beta,2}(r, \beta, z)\big|_{r=r_1} \\ B_{r,1}(r, \beta, z)\big|_{r=r_1} = B_{r,2}(r, \beta, z)\big|_{r=r_1} \end{cases}$$
$$\begin{cases} H_{\beta,2}(r, \beta, z)\big|_{r=r_2} = H_{\beta,3}(r, \beta, z)\big|_{r=r_2} \\ B_{r,2}(r, \beta, z)\big|_{r=r_2} = B_{r,3}(r, \beta, z)\big|_{r=r_2}. \end{cases} \quad (42)$$

For $r = r_0$:

According to boundary conditions, the expression for the $^{\xi,\kappa}C_6$ constant can be derived as

$$^{\xi,\kappa}C_6 = \frac{I_{\xi-1}(^{\kappa}k_1 \cdot r_0) + I_{\xi+1}(^{\kappa}k_1 \cdot r_0)}{K_{\xi-1}(^{\kappa}k_1 \cdot r_0) + K_{\xi+1}(^{\kappa}k_1 \cdot r_0)}. \quad (43)$$

For $r = r_1$ and r_2, according to boundary conditions, the $^{\xi,\kappa}C_5$, $^{\xi,\kappa}C_7$, $^{\xi,\kappa}C_8$, and $^{\xi,\kappa}C_9$ constant can be derived, which are shown in Appendix I.

Therefore, the non-slotted 3-D radial air-gap flux density can be calculated as

$$^{\xi,\kappa}B_{r,1}(r, \beta, z) = \frac{1}{r}\left[\frac{\partial}{\partial\beta}\left({}^{\xi,\kappa}A_{z,1}\right) - \frac{\partial}{\partial z}\left(r \cdot {}^{\xi,\kappa}A_{\beta,1}\right)\right]\Big|_{r=r_0}. \quad (44)$$

According to (24) and (25), the constants have been calculated, and then, (44) can be derived

$$^{\xi,\kappa}B_{r,1}(r, \beta, z) = -j\frac{r_0}{\xi}\left[\left(\frac{\xi}{r_0}\right)^2 + \left(\frac{\kappa\pi}{L}\right)^2\right]$$
$$\cdot {}^{\xi,\kappa}C_5 \cdot \left[I_{\xi}(k_1 \cdot r_0) + {}^{\xi,\kappa}C_6 \cdot K_{\xi}(k_1 \cdot r_0)\right]$$
$$\cdot {}^{\kappa}a \cdot \cos\left(\kappa\frac{\pi}{L}z\right) \cdot e^{-j\xi\beta}. \quad (45)$$

In analogy, the non-slotted 3-D tangential air-gap flux density can be calculated as

$$^{\xi,\kappa}B_{\beta,1}(r, \beta, z)$$
$$= \left[\frac{\partial}{\partial z}\left({}^{\xi,\kappa}A_{r,1}\right) - \frac{\partial}{\partial r}\left({}^{\xi,\kappa}A_{z,1}\right)\right]\Big|_{r=r_0}$$
$$= -\frac{k1}{2} \cdot {}^{\xi,\kappa}C_5 \cdot \left\{ \begin{array}{l} I_{\xi-1}(k_1 \cdot r_0) + I_{\xi+1}(k_1 \cdot r_0) \\ -{}^{\xi,\kappa}C_6 \cdot \left[K_{\xi-1}(k_1 \cdot r_0) + K_{\xi+1}(k_1 \cdot r_0)\right] \end{array} \right\}$$
$$\cdot {}^{\kappa}a \cdot \cos\left(\kappa\frac{\pi}{L}z\right) \cdot e^{-j\xi\beta}. \quad (46)$$

Furthermore, for the equivalent SPM machine, the process of circumferential and axial modeling gives a general view of how to conduct magnetic analysis of machines with axial segmented technique. Compared to machines with and without axial segmented technique, the difference exists only in the axial modeling of MMF. For the axial modeling, the phase of MMF changes with axial position, but the amplitude of MMF keeps constant. Therefore, the non-slotted air-gap flux density of machines with the axial segmented technique needs to only make the corresponding corrections to the phases in (45) and (46).

IV. SIMULATION RESULTS AND DISCUSSION

In order to verify the equivalent model and analytical model, the non-slotted radial and tangential air-gap flux density of four rotor topologies with four-pole/24-slot IPM machines are obtained by FEM, which works as the reference. The structural parameters of four IPM machines are shown in Tables II–IV.

The open-loop non-slotted radial air-gap flux density of four IPM topologies is shown in Fig. 8. As to overview, the air-gap flux density of the analytical method agrees well with those of the FEM in four IPM topology cases. It should be noted that: 1) negligible fluctuation of the analytical method is caused by the finite calculated circumferential harmonic order, which is only calculated to the 15th order, and 2) comparing the three single-layer IPM topologies, the tangentially IPM has the largest air-gap flux density amplitude. The reasons are given as follows: 1) The same reluctance, and 2) the larger MMF. For MMF, according to (2) and (3), the different magnet pole-arc widths cause different amplitudes of MMF. Due to the smallest magnet pole-arc width in tangential IPM topology, the MMF is the largest. As to the ribs, the parameters of ribs reflect on the magnet pole-arc width and have been contained in the magnet pole-arc of four IPM topologies. 3) In the double-layer V-shaped IPM topology, the amplitude of first-layer flux density calculated by an analytical method is lower than that of FEM. A couple of reasons are given as follows: 1) the larger magnet pole-arc width and 2) the larger equivalent air-gap length. For the magnet pole-arc width, the higher amplitude of first-layer

$$^{\xi,\kappa}R_{2P} = -\frac{1}{\kappa k_2}\left\{ \begin{array}{l} I_{\xi}(^{\kappa}k_2 \cdot r) \cdot \left[2\sum_{n=0}^{(\xi-3)/2}(-1)^{n+1} \cdot K_{\xi-2n-1}(^{\kappa}k_2 \cdot r) + (-1)^{(\xi-3)/2} \cdot K_0(^{\kappa}k_2 \cdot r)\right] \\ -K_{\xi}(^{\kappa}k_2 \cdot r) \cdot \left[2\sum_{n=0}^{(\xi-3)/2}(-1)^{n} \cdot I_{\xi-2n-1}(^{\kappa}k_2 \cdot r) + (-1)^{(\xi-1)/2} \cdot I_0(^{\kappa}k_2 \cdot r)\right] \end{array} \right\} \quad (38)$$
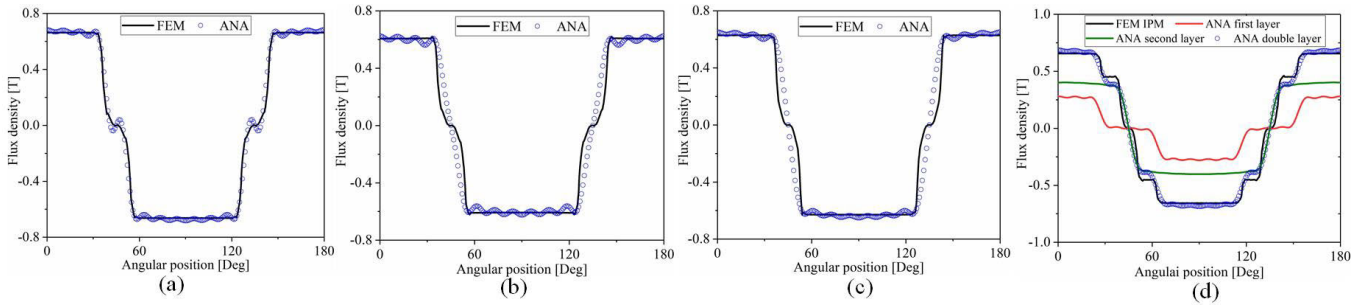
Fig. 8. Radial air-gap flux density. (a) Tangentially IPM. (b) Multi-segment tangentially IPM. (c) Single-layer V-shaped PM. (d) Double-layer V-shaped PM.
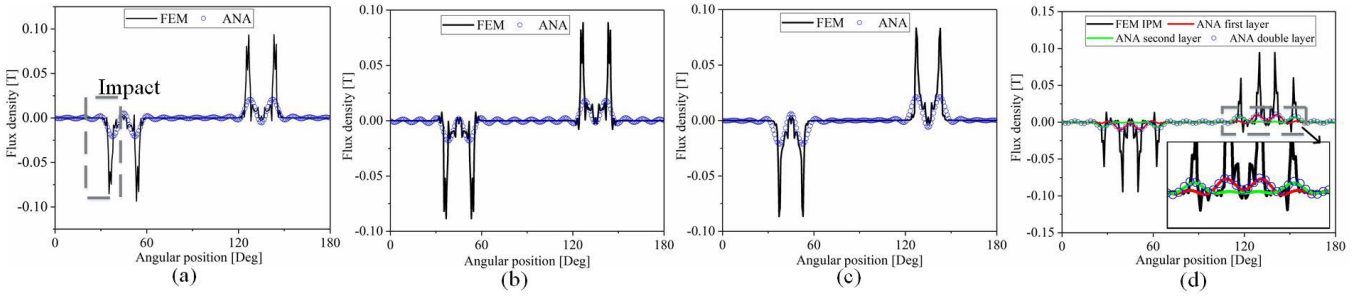

Fig. 9. Tangential air-gap flux density. (a) Tangentially IPM. (b) Multi-segment tangentially IPM. (c) Single-layer V-shaped PM. (d) Double-layer V-shaped PM.
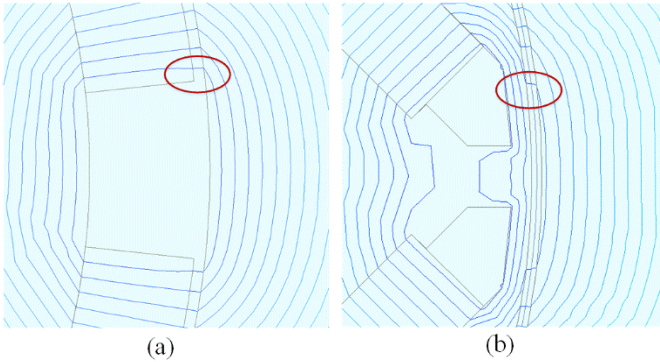

Fig. 10. Slotless air-gap field distribution. (a) SPM machine. (b) IPM machine.

IPM causes relevant equivalent SPM with a smaller thickness. Meanwhile, due to the existence of double-layer IPM, the air-gap length of the equivalent SPM machine is larger, but the measured air-gap point is not changed. Therefore, there is a large magnetic pressure drop within the air gap. The amplitude of air gap flux density on the second-layer equivalent SPM surface is in agreement with that of FEM.

The open-loop non-slotted tangential air-gap flux density for four IPM topologies is shown in Fig. 9. Compared with FEM, we can get: 1) as to overview, the horizontal waveform of the analytical model is consistent with that of FEM except for the impact and 2) specifically, for the impact of the waveform, the analytical model cannot match well with the FEM. The flux lines of the slotless air-gap field distribution of IPM machine and SPM machine are shown in Fig. 10. Flux enters the air gap with a certain slope at the edge of the magnet pole arc in IPM machine, which causes a large amplitude of tangential flux density at the edge of

the pole arc, and the amplitude of tangential flux density is proportional to the slope. However, flux enters the air gap almost vertically at the edge of the magnet pole arc in SPM, which leads to a mismatch between the analytical method and the FEM. In Section V, this impact is considered in detail.

Furthermore, the influence of the thickness and the layer change of the IPM on the accuracy of equivalent model and analytical method are studied, and the V-shaped IPM is chosen as the test machine. This is because V-shaped IPM is widely used. The non-slotted radial air-gap flux density under different PM thicknesses is shown in Fig. 11. Here, the thickness of IPM is 4 and 6 mm. It should be noted that only the thickness of PM is changed. Meanwhile, the non-slotted radial air-gap flux density of three-layer V-shaped IPM is shown in Fig. 12, where the thickness of third layer IPM is 1 mm. Obviously, the waveforms of analytical method can match well with that of FEM in each case. Specifically, the first layer IPM of analytical model does not match FEM in a three-layer IPM case. The reason is similar to that of double-layer IPM case. For the three-layer IPM, compared with other layer magnets, the first layer magnet has a larger pole-arc width, which causes the smaller thickness of the equivalent magnet. Meanwhile, due to the three-layer magnet, the equivalent air-gap length is significantly large, but the measured air-gap point is not changed during the equivalent process, which results in a large magnetic pressure drop in the air gap in the first-layer equivalent process. However, the error of the first layer magnet does not affect the overview distribution. In a word, the equivalent model and the analytical method can well solve the air-gap flux density of IPM machines.

In addition, a comparative study is conducted. The non-slotted air-gap flux density of this article and [17] is shown
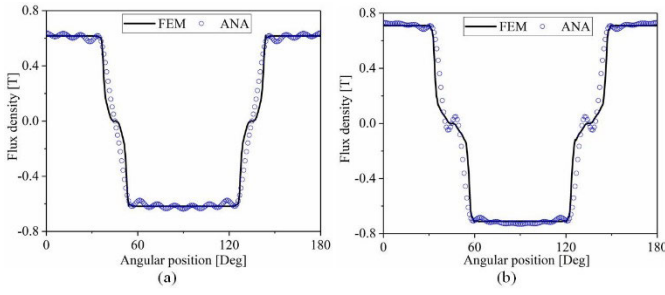
Fig. 11. Air-gap radial flux density under different PM thicknesses. (a) 4 mm. (b) 6 mm.
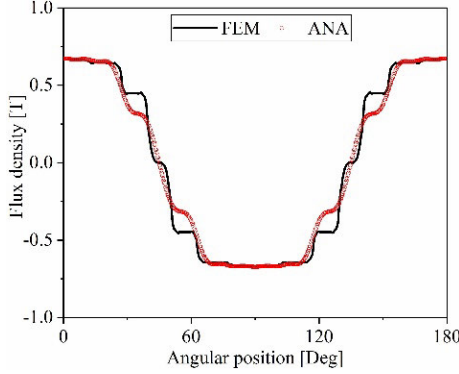

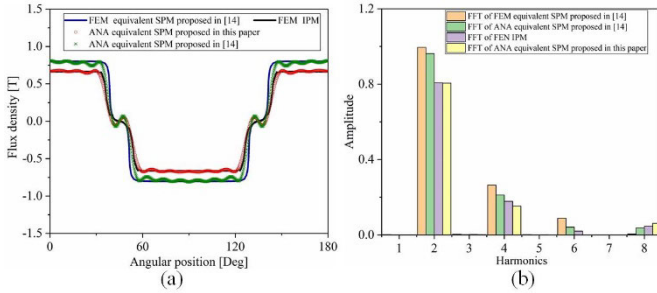Fig. 12. Radial air-gap flux density of three-layer V-shaped IPM.

Fig. 13. Non-slotted radial flux density and FFT. (a) Flux density of this article or [17]. (b) FFT.

in Fig. 13. We can get: 1) the amplitude of flux density of analytical method proposed in [17] is higher than the result of FEM and 2) the waveform of analytical method proposed in this article is consistent with FEM in the IPM case. This is because the amplitude of k_{mag} equals one in (2) in [17], that is, as long as the thickness of the PM remains unchanged, the MMF is guaranteed to be constant during the equivalent process. Compared with the equivalent rotor model in [17], the equivalent rotor model proposed in this article is more accurate.

V. SALIENCY AND SLOTTING EFFECTS

Since the slotting effect cannot be considered in Maxwell's equation-based 3-D analytical model, the slotting effect is the core of this section. Meanwhile, the non-slotted tangential flux density of analytical method does not match with FEM in
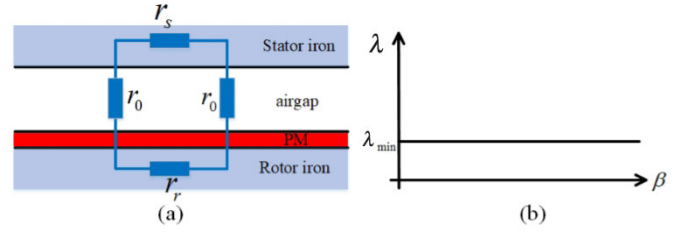

Fig. 14. Flux-path permeance function of equivalent SPM. (a) Magnetic loop model. (b) Flux-path permeance function.

Section IV, and thus, the saliency coefficient is proposed to correct.

A. Saliency Effect

In order to solve the problem that the non-slotted tangential flux density of analytical model does not match that of FEM, thus the saliency effect needs to be considered. For the IPM machine, due to the magnetic resistance difference of dq-axis, the saliency effect exists in this topology motor but cannot be considered in the rotor topology equivalent process.

To solve the equivalent error, a new analytical method is presented, and then, the saliency coefficient is derived. In this model, the air-gap flux density is based on the MMF and flux-path permeance function.

The flux loop and permeance function of the equivalent SPM rotor topology is shown in Fig. 14. Due to the uniform equivalent air-gap length, the amplitude of permeance is constant, which can be calculated by

$$\lambda_{\min} = \frac{1}{2 \cdot r_0 + r_s + r_r} \tag{47}$$

where r_0 is equivalent air-gap reluctance and r_s and r_r are stator and rotor reluctance, respectively, which can be calculated by

$$\begin{aligned} r_0 &= \frac{h'_m}{\mu_0} + \frac{g'}{\mu_0} \\ r_s &= \frac{l_{s\_\mathrm{Yoke}}}{\mu_r \mu_0} \\ r_r &= \frac{l_{r\_\mathrm{Yoke}}}{\mu_r \mu_0} \end{aligned} \tag{48}$$

where l_{r_Yoke} and l_{s_Yoke} are, respectively, the circumferential flux loop length along with the rotor and stator yoke

$$\lambda_{\max} = \frac{1}{2 \cdot r_1 + r_s + r_r}. \tag{49}$$

With

$$r_1 = \frac{g'}{\mu_0} + \frac{h'_m}{\mu_r \cdot \mu_0}. \tag{50}$$

The flux-path permeance function of the IPM is shown in Fig. 15. From Fig. 15, we can get: 1) through stator core, air gap, PM, and rotor core, the flux loop is formed and consistent with that in the SPM rotor topology, which leads to the same amplitude of low permeance and 2) through stator core, air gap, and rotor core, another flux loop is formed and different from that in the SPM rotor topology, which causes that the
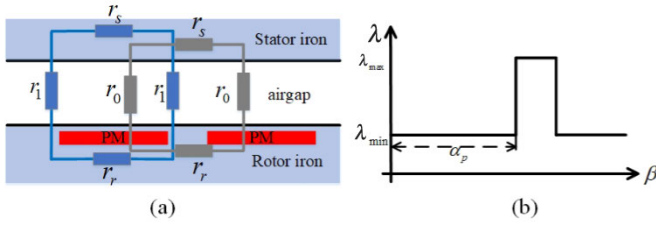
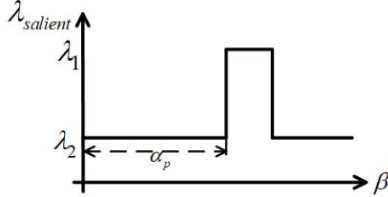Fig. 15. Flux-path permeance function of IPM. (a) Magnetic loop model. (b) Flux-path permeance function.

Fig. 16. Saliency coefficient function.

amplitude of permeance is higher than that of the flux loop through PM.

According to the MMF and flux-path permeance model, the air-gap flux density is expressed as

$$B_{\text{airgap}} = \text{MMF} \cdot \lambda. \tag{51}$$

Therefore, the air-gap flux density of the equivalent SPM machine is

$$B_{\text{airgap\_SPM}} = \text{MMF} \cdot \lambda_{\text{SPM}}. \tag{52}$$

In analogy, the air-gap flux density of the IPM machine is

$$B_{\text{airgap\_IPM}} = \text{MMF} \cdot \lambda_{\text{IPM}}. \tag{53}$$

Due to the unchanged amplitude of MMF in the same topology, only the flux-path permeance function difference exists between the IPM and equivalent SPM rotor topology. In order to accurately calculate tangential air-gap flux density, the saliency coefficient λ_{salient} is introduced, which can be expressed as

$$\lambda_{\text{salient}} = \frac{\lambda_{\text{IPM}}}{\lambda_{\text{SPM}}}. \tag{54}$$

The saliency coefficient function is shown in Fig. 16, in which a couple of points are demonstrated: 1) under the premise that the constant total length of air gap and PM, λ_2 is equal to one and 2) $\lambda_1 = \lambda_{\text{max}}/\lambda_{\text{min}}$. The saliency coefficient can be expressed by the Fourier series

$$\lambda_{\text{salient}}(\beta) = \lambda_0 + \sum_{n=1}^{\infty} \lambda_n \cdot e^{-j \cdot 2n \cdot \beta}. \tag{55}$$

With

$$\lambda_0 = \frac{\lambda_1 \cdot (\pi - \alpha_p \cdot \pi) + \lambda_2 \cdot (\alpha_p \cdot \pi)}{\pi} \tag{56}$$

$$\lambda_n = \frac{2}{\pi} \frac{(\lambda_1 - \lambda_2) \cdot \sin(n\alpha_p)}{n} \tag{57}$$

where λ_0 and λ_n represent the Fourier coefficient and n is the harmonics order.

TABLE I
HARMONIC COMPONENT OF OPEN-CIRCUIT AIR-GAP FLUX DENSITY

PM topology	Spatial order
Equivalent SPM	ξ
IPM	$\xi \pm 2n$

Therefore, the non-slotted tangential air-gap flux density considering the saliency effect can be expressed as

$$^{\xi,\kappa} B_{\beta s}(r, \beta, z) = {}^{\xi,\kappa} B_{\beta}(r, \beta, z) \cdot \lambda_{\text{salient}} \tag{58}$$

where $^{\xi,\kappa} B_{\beta s}(r, \beta, z)$ is the tangential components of air-gap flux density with saliency effect.

According to (58), the harmonic component of open-circuit flux density of the IPM machine is shown in Table I. Compared with the equivalent SPM and IPM, we can get the following.

1) The saliency effect does not generate new spatial order harmonics. This is because the value of ξ and n is the odd number and natural number, i.e., the amplitude of ξ includes $\xi \pm 2n$.

2) The effect of the saliency effect on the open-circuit air-gap flux density is to change the harmonic amplitude.

Meanwhile, for four different IPM topologies, the non-slotted tangential air-gap flux density considering saliency effect is shown in Fig. 17. As to overview, the waveform of analytical model can match well with that of FEM through the saliency coefficient correction.

B. Slotting Effect

Due to the neglected slotting effect in Maxwell's equation-based 3-D analytical model, it is considered by the complex relative permeance, which works as an additional function. The slotting effect can be demonstrated as

$$\lambda^*(\beta) = \lambda_a + j\lambda_b \tag{59}$$

where λ_a and λ_b, respectively, present the real part and imaginary part, which can be expressed by the Fourier series as

$$\begin{cases} \lambda_a = \lambda_{a0} + \sum_{m=1}^{\infty} \lambda_{am} \cos(m \cdot Q_s \alpha) \\ \lambda_b = \sum_{m=1}^{\infty} \lambda_{bm} \sin(m \cdot Q_s \alpha) \end{cases} \tag{60}$$

where λ_{a0} and λ_{am} denote the constant and coefficient of the real part, respectively, λ_{bm} is the coefficient of the imaginary part, and Q_s is the number of stator slot.

Due to $^{\xi,\kappa} B_{\text{airgap}} = {}^{\xi,\kappa} B_{rs} + j \cdot {}^{\xi,\kappa} B_{\beta s}$, the radial and tangential air-gap flux density are calculated as

$$\begin{cases} ^{\xi,\kappa} B_{rss}(r, \beta, z) = {}^{\xi,\kappa} B_{rs}(r, \beta, z)\lambda_a + {}^{\xi,\kappa} B_{\beta s}(r, \beta, z)\lambda_b \\ ^{\xi,\kappa} B_{\beta ss}(r, \beta, z) = {}^{\xi,\kappa} B_{\beta s}(r, \beta, z)\lambda_a - {}^{\xi,\kappa} B_{rs}(r, \beta, z)\lambda_b \end{cases} \tag{61}$$

where $^{\xi,\kappa} B_{rss}(r, \beta, z)$ and $^{\xi,\kappa} B_{\beta ss}(r, \beta, z)$ are the radical and tangential air-gap flux density considering saliency and slotting effect, respectively.

Considering the slotting effect, the radial and tangential air-gap flux density of four typical IPM topologies are shown
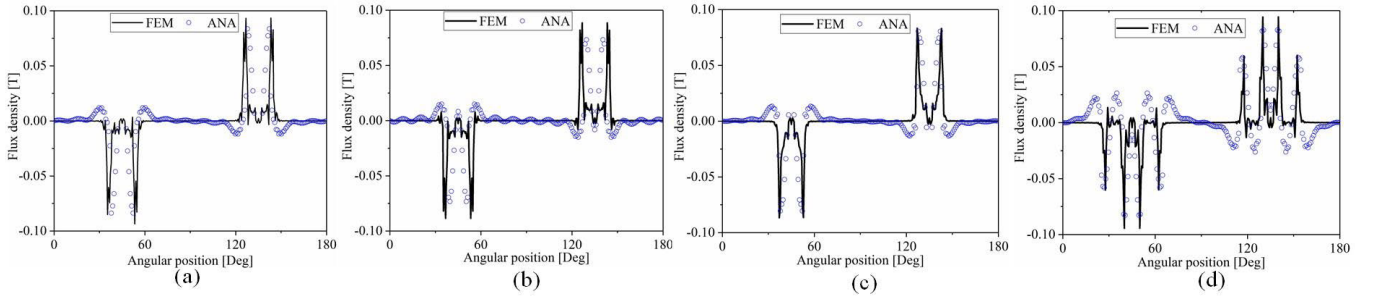
Fig. 17. Tangential air-gap flux density. (a) Tangentially IPM. (b) Multi-segment tangentially IPM. (c) Single-layer V-shaped PM. (d) Double-layer V-shaped PM.
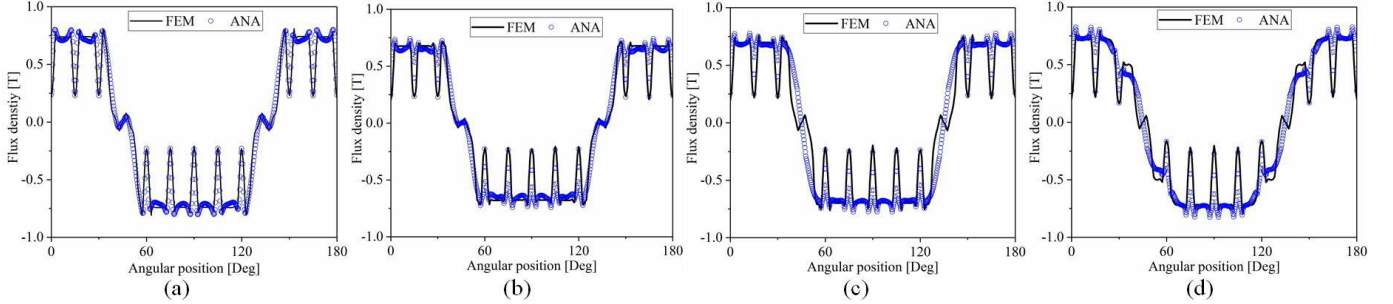

Fig. 18. Radial air-gap flux density. (a) Tangentially IPM. (b) Multi-segment tangentially IPM. (c) Single-layer V-shaped PM. (d) Double-layer V-shaped PM.
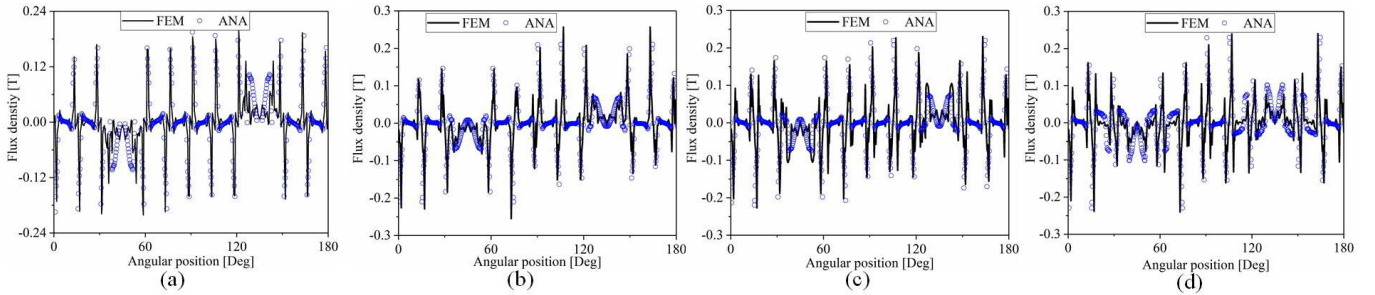

Fig. 19. Tangential air-gap flux density. (a) Tangentially IPM. (b) Multi-segment tangentially IPM. (c) Single-layer V-shaped PM. (d) Double-layer V-shaped PM.

in Figs. 18 and 19, respectively. It should be noted that the parameters of stator and slots are the same in different IPM topologies and shown in Table I. For the radial flux density, regardless of the IPM topology, the result calculated by the analytical method agrees well with that of FEM, because in the case of no slot, the result has been consistent with that of FEM. For the tangential flux density, since the saliency effect has been considered, waveforms of analytical method and FEM are consistent. In the case of considering the slotting effect, the equivalent model and analytical model can be well components to calculate the air-gap flux density of different IPM topology machines.

VI. CONCLUSION

This article proposes a general analytical model to conduct the 3-D magnetic analysis of the IPM machine by coupling the equivalent rotor equivalent and Maxwell's equation-based 3-D analytical model. To reduce the complex boundary conditions,

the IPM topology can be equivalent to the SPM topology by the rotor equivalent model, which is suitable for various IPM topologies. Meanwhile, the equivalent principle is constant reluctance and MMF. As to the ribs, the parameters are reflected on magnet pole-arc width and can be considered during the equivalent process. Then, the 3-D analytical model is established to conduct the magnetic analysis and obtain the uniform expression of open-circuit air-gap flux density. This 3-D analytical model is in particular suitable for electrical machines with axial segmented technique.

For the non-slotted radial flux density, we can get: 1) as to overview, the waveforms of the analytical model can match well with those of FEM, despite the different IPM topologies, thickness and layer, and 2) the different flux density amplitudes of single-layer IPM topologies are caused by different magnet pole-arc widths. The larger the magnet pole-arc width, the lower the flux density. For the non-slotted tangential air-gap flux density, the result of analytical model is consistent

TABLE II
MAIN AND COMMON PARAMETER OF TEST MACHINES

Parameter	Symbol	Value
Rated Power (kW)	-	0.55
Rated speed (rpm)	-	3600
PM material	-	XG196/96
Pole /slot	$2p/Q_s$	4/24
Stator inner bore radius (mm)	R_s	37.5
Rotor outer bore radius (mm)	R_r	37
Airgap length (mm)	g	0.5
Slot opening height (mm)	h_{s0}	0.5
Slot wedge height (mm)	h_{s1}	1
Slot body height (mm)	h_{s2}	8.2
Slot opening width (mm)	b_{s0}	2.5
Slot wedge maximum width (mm)	b_{s1}	5.6
Shaft diameter (mm)	-	26
Axial length (mm)	L	65
Magnetizing direction	-	Parallel

TABLE III
DIFFERENT PARAMETERS OF SINGLE-LAYER IPM STRUCTURE

Parameter	Tangentially IPM	Multi-segment tangentially IPM	Single-layer V-shaped IPM
PM thickness (mm)	$h_m=5$	$h_m=5$	$h_m=5$
PM width (mm)	$W_{mag}=40$	$W_{mag1}+W_{mag2}=40$	$W_{mag}=40$
Distance from duct bottom to shaft surface	$O_2=12$	$O_2=3$	$O_2=3$
Pole-arc width	$\alpha_p=0.86$	$\alpha_p=0.94$	$\alpha_p=0.9$
Rib width	$W_{rib}=3$	$W_{rib}=3$	$W_{rib}=3$

TABLE IV
DIFFERENT PARAMETERS OF DOUBLE-LAYER IPM STRUCTURE

Parameter	Double-layer V-shaped IPM
First-layer PM thickness (mm)	$h_{m1}=3$
First-layer PM width (mm)	$W_{mag1}=40$
Second-layer PM thickness (mm)	$h_{m2}=2$
Second-layer PM width (mm)	$W_{mag2}=30$
Distance from first-layer duct bottom to shaft surface	$O_2=3$
Distance from second-layer duct bottom to shaft surface	$O_2=10$
First-layer pole-arc width	$\alpha_{p1}=0.9$
Second-layer pole-arc width	$\alpha_{p2}=0.6$

with that of FEM, except for impact, which is caused by the saliency effect. For the saliency effect, it is considered by the saliency coefficient, which is derived based on the MMF and flux-path permeance function and can well solve the error of non-slotted tangential flux density. As to slotted flux density, the waveforms between analytical model and FEM are consistent under different IPM topologies. Hence, a general analytical model has been proven to study well the open-circuit flux density of machines with different IPM topologies.

Moreover, the influence of saliency effect on harmonic order of the open-circuit air-gap flux density can guide the subsequent armature reaction magnetic analysis of the IPM machine. This is critical for the research of vibration and noise of the IPM machine. Based on the open-circuit air-gap flux density solved in this article, the 3-D electromagnetic characteristics of IPM machine can be obtained, which can consider the end effect.

Tables II–IV show the structural parameters of the four IPM topology machines.

APPENDIX I

According to the boundary conditions between air gap and PM, and PM and rotor core, the constants $^{\xi,\kappa}C_5$, $^{\xi,\kappa}C_7$, $^{\xi,\kappa}C_8$, and $^{\xi,\kappa}C_9$ can be calculated as (A-1)–(A-3), shown at the bottom of the page.

$$^{\xi,\kappa}C_7 = \frac{^{\xi,\kappa}C_8 \left\{ \begin{array}{l} K_\xi(^\kappa k_2 \cdot r_1) \cdot D(k_1 \cdot r_1) \\ + \frac{k_2}{k_1}\frac{\mu_1}{\mu_2}\left[\begin{array}{l} I_{\xi-1}(^\kappa k_2 \cdot r_1)+ \\ I_{\xi+1}(^\kappa k_2 \cdot r_1) \end{array}\right] \cdot G(k_1 \cdot r_1) \end{array} \right\} + R_{3P}(^\kappa k_2 \cdot r_1) \cdot D(k_1 \cdot r_1) - \frac{k_2}{k_1}\frac{\mu_1}{\mu_2}\frac{2}{k_2}R'_{3P}(^\kappa k_2 \cdot r_1) \cdot G(k_1 \cdot r_1)}{\frac{k_2}{k_1}\frac{\mu_1}{\mu_2}\left[\begin{array}{l} I_{\xi-1}(^\kappa k_2 \cdot r_1) \\ +I_{\xi+1}(^\kappa k_2 \cdot r_1) \\ \cdot G(k_1 \cdot r_1) \end{array}\right] - D(k_1 \cdot r_1) \cdot I_\xi(^\kappa k_2 \cdot r_1)} \tag{A-1}$$

$$\begin{cases} D(k_1 \cdot r_1) = \left[\begin{array}{l} I_{\xi-1}(^\kappa k_1 \cdot r_1) \\ +I_{\xi+1}(^\kappa k_1 \cdot r_1) \end{array}\right] - ^{\xi,\kappa}C_6 \cdot \left[\begin{array}{l} K_{\xi-1}(^\kappa k_1 \cdot r_1) \\ +K_{\xi+1}(^\kappa k_1 \cdot r_1) \end{array}\right] \\ G(k_1 \cdot r_1) = I_\xi(^\kappa k_1 \cdot r_1) + ^{\xi,\kappa}C_6 \cdot K_\xi(^\kappa k_1 \cdot r_1) \end{cases} \tag{A-2}$$

$$^{\xi,\kappa}C_8 = \frac{\left[\begin{array}{l} \frac{k_2}{k_1}\frac{\mu_1}{\mu_2}\frac{2}{k_2}R'_{3P} \cdot G(1,1) \\ +R_{3P} \cdot D(1,1) \end{array}\right] \cdot \left[\begin{array}{l} \frac{k_2}{k_3}\frac{\mu_3}{\mu_2}A(2,2) \cdot I_\xi(k_3 \cdot r_2) \\ -I_\xi(k_2 \cdot r_2) \cdot A(3,2) \end{array}\right] + \left[\begin{array}{l} -\frac{k_2}{k_3}\frac{\mu_3}{\mu_2}\frac{2}{k_3}R'_{3P} \\ +R_{3P} \cdot A(3,2) \end{array}\right] \cdot \left[\begin{array}{l} \frac{k_2}{k_1}\frac{\mu_1}{\mu_2} \cdot A(2,1) \cdot G(1,1) \\ -I_\xi(k_2 \cdot r_1) \cdot D(1,1) \end{array}\right]}{\left[\begin{array}{l} K_\xi(k_2 \cdot r_1) \cdot D(1,1) \\ +\frac{k_2}{k_1}\frac{\mu_1}{\mu_2} \cdot A(2,1) \cdot G(1,1) \end{array}\right] \cdot \left[\begin{array}{l} \frac{k_2}{k_3}\frac{\mu_3}{\mu_2}A(2,2) \cdot I_\xi(k_3 \cdot r_2) \\ -I_\xi(k_2 \cdot r_2) \cdot A(3,2) \end{array}\right] - \left[\begin{array}{l} I_\xi(k_2 \cdot r_2) \cdot A(3,2) \\ +\frac{k_2}{k_3}\frac{\mu_3}{\mu_2} \cdot B(2,1) \cdot I_\xi(k_3 \cdot r_2) \end{array}\right] \cdot \left[\begin{array}{l} \frac{k_2}{k_1}\frac{\mu_1}{\mu_2} \cdot A(2,1) \cdot G(1,1) \\ -I_\xi(k_2 \cdot r_1) \cdot D(1,1) \end{array}\right]} \tag{A-3}$$

With

$$A(3, 2) = I_{\xi-1}(k_3 \cdot r_2) + I_{\xi+1}(k_3 \cdot r_2)$$

$$B(2, 2) = K_{\xi-1}(k_2 \cdot r_2) + K_{\xi+1}(k_2 \cdot r_2)$$

$$A(2, 2) = I_{\xi-1}(k_2 \cdot r_2) + I_{\xi+1}(k_2 \cdot r_2) \tag{A-4}$$

$$^{\xi,\kappa}C_9 = -j \frac{\mu_0 {}^{\xi}M^{\Delta} \begin{bmatrix} {}^{\xi,\kappa}C_7 \cdot I_{\xi}(k_2 \cdot r_2) \\ + {}^{\xi,\kappa}C_8 \cdot K_{\xi}(k_2 \cdot r_2) + R_{3P} \end{bmatrix}}{I_{\xi}(k_3 \cdot r_2)} \tag{A-5}$$

$$^{\xi,\kappa}C_5 = -j \frac{\mu_0 {}^{\xi}M^{\Delta} \cdot \begin{bmatrix} {}^{\xi,\kappa}C_7 \cdot I_{\xi}(k_2 \cdot r_1) \\ + {}^{\xi,\kappa}C_8 \cdot k_{\xi}(k_2 \cdot r_1) + R_{3P} \end{bmatrix}}{I_{\xi}(k_1 \cdot r_1) + {}^{\xi,\kappa}C_6 \cdot K_{\xi}(k_1 \cdot r_1)}. \tag{A-6}$$

ACKNOWLEDGMENT

REFERENCES

[1] A. M. El-Refaie et al., "Advanced high-power-density interior permanent magnet motor for traction applications," *IEEE Trans. Ind. Appl.*, vol. 50, no. 5, pp. 3235–3248, Sep./Oct. 2014.

[2] Y. Miao, H. Ge, M. Preindl, J. Ye, B. Cheng, and A. Emadi, "MTPA fitting and torque estimation technique based on a new flux-linkage model for interior-permanent-magnet synchronous machines," *IEEE Trans. Ind. Appl.*, vol. 53, no. 6, pp. 5451–5460, Nov./Dec. 2017.

[3] S. Abdi, E. Abdi, H. Toshani, and R. McMahon, "Vibration analysis of brushless doubly fed machines in the presence of rotor eccentricity," *IEEE Trans. Energy Convers.*, vol. 35, no. 3, pp. 1372–1380, Sep. 2020.

[4] S.-M. Hwang, K.-T. Kim, W.-B. Jeong, Y.-H. Jung, and B.-S. Kang, "Comparison of vibration sources between symmetric and asymmetric HDD spindle motors with rotor eccentricity," *IEEE Trans. Ind. Appl.*, vol. 37, no. 6, pp. 1727–1731, Nov./Dec. 2001.

[5] Y. Li, Q. Lu, Z. Q. Zhu, L. J. Wu, G. J. Li, and D. Wu, "Analytical synthesis of air-gap field distribution in permanent magnet machines with rotor eccentricity by superposition method," *IEEE Trans. Magn.*, vol. 51, no. 11, pp. 1–4, Nov. 2015.

[6] Z. Zhang, C. Xia, Y. Yan, Q. Geng, and T. Shi, "A hybrid analytical model for open-circuit field calculation of multilayer interior permanent magnet machines," *J. Magn. Magn. Mater.*, vol. 435, pp. 136–145, Aug. 2017.

[7] L. Zhu, S. Z. Jiang, Z. Q. Zhu, and C. C. Chan, "Analytical modeling of open-circuit air-gap field distributions in multisegment and multilayer interior permanent-magnet machines," *IEEE Trans. Magn.*, vol. 45, no. 8, pp. 3121–3130, Aug. 2009.

[8] E. Schmidt, M. Sušć, and A. Eilenberger, "Finite element analysis of a permanent magnet synchronous machine with an external rotor for a position sensorless control," in *Proc. Australas. Universities Power Eng. Conf.*, 2009, pp. 1–6.

[9] S. Ruoho, E. Dlala, and A. Arkkio, "Comparison of demagnetization models for finite-element analysis of permanent-magnet synchronous machines," *IEEE Trans. Magn.*, vol. 43, no. 11, pp. 3964–3968, Nov. 2007.

[10] M. B. Fauchez, "Magnetic analysis of a switched reluctance motor using a boundary element-finite element coupling method," *IEEE Trans. Magn.*, vol. MAG-24, no. 1, pp. 475–478, Jan. 1988.

[11] X. Zhu, W. Wu, L. Quan, Z. Xiang, and W. Gu, "Design and multi-objective stratified optimization of a less-rare-earth hybrid permanent magnets motor with high torque density and low cost," *IEEE Trans. Energy Convers.*, vol. 34, no. 3, pp. 1178–1189, Sep. 2019.

[12] X. Zhu, Z. Xiang, L. Quan, Y. Chen, and L. Mo, "Multimode optimization research on a multiport magnetic planetary gear permanent magnet machine for hybrid electric vehicles," *IEEE Trans. Ind. Electron.*, vol. 65, no. 11, pp. 9035–9046, Nov. 2018.

[13] L. Ding, G. Liu, Q. Chen, and G. Xu, "A novel mesh-based equivalent magnetic network for performance analysis and optimal design of permanent magnet machines," *IEEE Trans. Energy Convers.*, vol. 34, no. 3, pp. 1337–1346, Sep. 2019.

[14] Z. Q. Zhu, D. Howe, E. Bolte, and B. Ackermann, "Instantaneous magnetic field distribution in brushless permanent magnet DC motors. I. Open-circuit field," *IEEE Trans. Magn.*, vol. 29, no. 1, pp. 124–135, Jan. 1993.

[15] L. Jing, W. Tang, T. Wang, T. Ben, and R. Qu, "Performance analysis of magnetically geared permanent magnet brushless motor for hybrid electric vehicles," *IEEE Trans. Transport. Electrific.*, vol. 8, no. 2, pp. 2874–2883, Jun. 2022.

[16] Q. Yu and D. Gerling, "Analytical modeling of a canned switched reluctance machine with multilayer structure," *IEEE Trans. Magn.*, vol. 49, no. 9, pp. 5069–5082, Sep. 2013.

[17] M. S. Mirazimi and A. Kiyoumarsi, "Magnetic field analysis of multi-flux-barrier interior permanent-magnet motors through conformal mapping," *IEEE Trans. Magn.*, vol. 53, no. 12, pp. 1–12, Dec. 2017.

[18] H. Zhuang, S. Zuo, Z. Ma, Q. Yu, Z. Wu, and C. Liu, "Magnetic analysis of skew effect in surface-mounted permanent magnet machines with skewed slots," *IEEE Trans. Magn.*, vol. 58, no. 12, pp. 1–12, Dec. 2022.

[19] C. Ma, Y. An, H. Zhao, S. Guo, X. Yin, and H. Lu, "3-D analytical model and direct measurement method of ultra-thin open-circuit air-gap field of interior permanent magnet synchronous motor with multi-segmented skew poles and multi-layered flat wire windings for electric vehicle," *IEEE Trans. Energy Convers.*, vol. 35, no. 3, pp. 1316–1326, Sep. 2020.

[20] D. Žarko, D. Ban, and T. A. Lipo, "Analytical calculation of magnetic field distribution in the slotted air gap of a surface permanent-magnet motor using complex relative air-gap permeance," *IEEE Trans. Magn.*, vol. 42, no. 7, pp. 1828–1837, Jul. 2006.

[21] M. Wang, J. Zhu, L. Guo, J. Wu, and Y. Shen, "Analytical calculation of complex relative permeance function and magnetic field in slotted permanent magnet synchronous machines," *IEEE Trans. Magn.*, vol. 57, no. 3, pp. 1–9, Mar. 2021.

[22] Z. Q. Zhu, L. J. Wu, and Z. P. Xia, "An accurate subdomain model for magnetic field computation in slotted surface-mounted permanent-magnet machines," *IEEE Trans. Magn.*, vol. 46, no. 4, pp. 1100–1115, Apr. 2010.

[23] G. Dajaku and D. Gerling, "Stator slotting effect on the magnetic field distribution of salient pole synchronous permanent-magnet machines," *IEEE Trans. Magn.*, vol. 46, no. 9, pp. 3676–3683, Sep. 2010.